Two-Dimensional Nanoscale Imaging of Gadolinium Spins via Scanning Probe Relaxometry with a Single Spin in Diamond

M. Pelliccione, B. A. Myers, L. M. A. Pascal, A. Das, and A. C. Bleszynski Jayich*

Department of Physics and the California NanoSystems Institute, University of California, Santa Barbara, Santa Barbara, California 93106, USA

(Received 12 September 2014; published 25 November 2014)

Spin labeling of molecules with paramagnetic ions is an important approach for determining molecular structure; however, current ensemble techniques lack the sensitivity to detect few isolated spins. In this paper, we demonstrate two-dimensional nanoscale imaging of paramagnetic gadolinium compounds using scanning relaxometry of a single nitrogen-vacancy (NV) center in diamond. Gadopentetate dimeglumine attached to an atomic-force microscope tip is controllably interacted with and detected by the NV center by virtue of the fact that the NV exhibits fast relaxation in the fluctuating magnetic field generated by electron spin flips in the gadolinium. Using this technique, we demonstrate a reduction in the T_1 relaxation time of the NV center by over 2 orders of magnitude, probed with a spatial resolution of 20 nm. Our result exhibits the viability of the technique for imaging individual spins attached to complex nanostructures or biomolecules, along with studying the magnetic dynamics of isolated spins.

DOI: 10.1103/PhysRevApplied.2.054014

I. INTRODUCTION

Mapping the structure of biomolecules including proteins and nucleic acids is of significant importance, as the functionality of a biomolecule is directly related to its structure [1]. For decades, paramagnetic compounds, including gadolinium-based complexes such as Gd-DTPA (diethylene triamine pentaacetic acid), have been studied for their effect of reducing proton (T_1) spin-lattice relaxation times [2], making them widely used as nuclear-magnetic-resonance imaging (MRI) contrast agents [3–5]. However, with conventional MRI techniques, the spatial resolution of contrast imaging is typically limited to the micron scale [6–8]. High-field electron paramagnetic resonance has made possible nanometer-scale distance measurements between magnetically interacting Gd^{3+} spins tagged to proteins [9,10], but these approaches rely on a large ensemble of labeled molecules to obtain a measurable signal. A nanoscale scanning probe technique would enable nonaveraged distance measurements on individual spin-labeled molecules, as well as an investigation of the magnetic dynamics of an isolated spin system. In this paper, we demonstrate nanoscale imaging of Gd compounds using scanning relaxometry of a single nitrogen-vacancy (NV) center in diamond. The NV is an atomic-scale defect whose electronic spin, at ambient temperatures, exhibits several-millisecond-long longitudinal relaxation times and can be optically polarized and interrogated on the single defect level [11]. Together with its excellent photostability, biocompatibility, and noninvasiveness [12,13], these properties make the NV a viable sensor for detecting and imaging individual spins in biological environments [14] and studying their fluctuation dynamics [15,16].

Gadolinium (Gd^{3+}) ions are particularly interesting spin systems, as they have a large unpaired electron spin of $S = 7/2$ and fast spin dynamics in the gigahertz frequency range. These properties make Gd compounds particularly effective as MRI contrast agents [17], as the relaxation time of protons in water is reduced in the presence of Gd. Analogously, the significant level of Gd spin noise at the frequency of the NV zero-field splitting (2.87 GHz) reduces the NV spin-relaxation time T_1, depending on the proximity and concentration of Gd [18,19]. This susceptibility has inspired the technique of NV relaxometry to detect Gd spins. Few to single Gd spin sensitivities have been reported using single NV centers in nanodiamonds surrounded by a lipid bilayer [12] as well as with Gd compounds bonded to bulk diamond [20]. Relaxometry with NV centers has also enabled the detection of ferromagnetic proteins in ambient conditions [21,22]. In addition, T_1-based imaging of Gd-tagged cellular structures has been demonstrated using ensembles of NV centers with a spatial resolution of 500 nm [18], where the resolution is limited by the use of wide-field optical detection.

For molecular scale imaging, improvements in the spatial resolution and sensitivity of relaxometry measurements are necessary. This goal can be achieved by using NV-based scanning probe techniques. Scanning probes have already enabled nanoscale magnetic imaging using a variety of detection schemes, including static stray-field imaging [23–26], double electron-electron resonance (DEER) [27], and proton-magnetic-resonance imaging [28,29]. Relaxometry has the advantage of directly sensing

*Corresponding author.
ania@physics.ucsb.edu

electron spins, which have a magnetic moment nearly 3 orders of magnitude larger than proton spins sensed in NMR. In addition, relaxometry allows for the measurement of spins with T_1 times too short for DEER detection. Thus far, scanning T_1 relaxometry imaging has remained a challenge due to the requirement of stable shallow NV centers with long T_1 times, coupled with the lengthy data acquisition times and associated scanning probe drift during the measurement. In this work, we overcome these challenges and perform two-dimensional NV relaxation imaging of a nanoscale volume of Gd electronic spins attached to an atomic-force microscope (AFM) tip with 20-nm resolution. Furthermore, we show that with reasonable improvements, this technique is capable of the sensitivity required to image a single isolated Gd spin.

II. METHODS

As depicted schematically in Fig. 1, the scanning probe setup combines a tuning-fork-based AFM, a top-down confocal microscope, and bulk diamond containing NV centers near the surface. Gadolinium is attached to a silicon AFM tip by submerging the cantilever in a chelated Gd solution [gadopentetate dimeglumine in water (Magnevist), concentration 30 mM] for several minutes. Experiments are performed at ambient conditions and in the absence of an applied static magnetic field. During the measurement, the AFM is operated in tapping mode with a tapping amplitude of 1-nm rms. The detection scheme is all optical; the NV center is polarized into the $|m_s = 0\rangle$ state of the ground-state triplet with a nonresonant green laser pulse and is read out via spin-dependent photoluminescence during a subsequent laser pulse a time τ later [30], as depicted in Fig. 2(a). During the dark time τ, the NV polarization relaxes to an equilibrium mixed state of $|0\rangle$, $|+1\rangle$, and $|-1\rangle$ with a characteristic time of T_1. In the

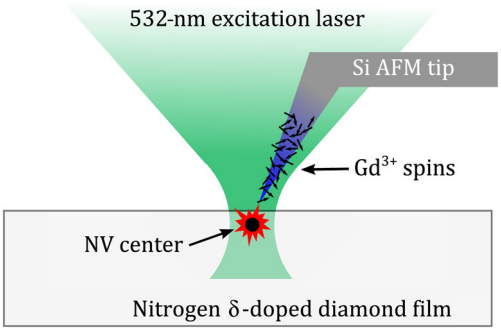

FIG. 1. Schematic of the scanning relaxometry measurement. A silicon AFM tip is coated with Gd compounds (Magnevist) and scanned near a shallow nitrogen-vacancy center in single-crystal diamond. A confocal microscope excites and polarizes the NV spin with a laser power of 437 μW and detects red photoluminescence to readout the NV spin polarization. This configuration allows for sensing a change in the NV spin-relaxation rate due to nearby Gd.

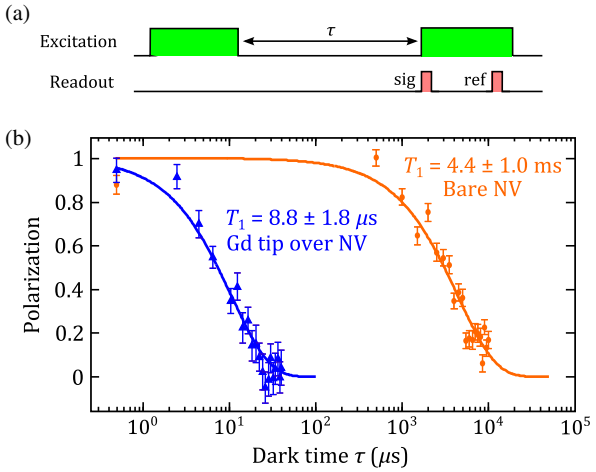

FIG. 2. (a) Pulse sequence used to measure the T_1 relaxation time, where the dark time τ is varied. Each signal pulse has a duration of 350 ns and is followed by a reference pulse after a delay of 2.5 μs. The dark time τ does not include a 500-ns dark time after the initialization pulse, which allows for full depopulation of the metastable state. (b) Measurement of spin relaxation of a single NV center with the Gd-coated AFM tip positioned over the NV center (blue triangles) and moved 5 μm away (orange circles). The vertical axis is plotted in terms of NV polarization with a polarization of 1 referring to the NV in the $|0\rangle$ state and a polarization of 0 referring to the NV in an equilibrium mixed state of $|0\rangle$, $|+1\rangle$, and $|-1\rangle$. The data are best fitted to an exponential decay (solid lines) with a single decay constant T_1.

presence of Gd a distance r from the NV, the NV T_1 is reduced according to the expression

$$T_1^{-1} = T_{1,\mathrm{int}}^{-1} + \Gamma_{\mathrm{Gd}}(r), \tag{1}$$

where $T_{1,\mathrm{int}}^{-1}$ is the intrinsic NV relaxation rate in the absence of Gd, and $\Gamma_{\mathrm{Gd}}(r)$ is the additional relaxation rate due to Gd. The NV is relaxed by magnetic fields perpendicular to its symmetry axis that appear static in the rotating frame, or, equivalently, that oscillate at the Larmor frequency $\omega_{\mathrm{NV}}/(2\pi) \approx 2.87$ GHz in the lab frame. Gadolinium has a magnetic noise spectral density that is broadened into the GHz range [18], and, hence, for sufficiently small r and sufficiently long $T_{1,\mathrm{int}}$, Γ_{Gd} can be of the same order or larger than $T_{1,\mathrm{int}}^{-1}$, leading to a detectable change in the NV T_1.

The diamond film in this work is grown with a nitrogen δ-doping method, in which nitrogen is incorporated into the diamond sample during epitaxial growth [31,32]. Growth is followed by electron irradiation and annealing for vacancy creation and diffusion [31]. The NV centers are 8–10 nm below the diamond surface, as determined by magnetic-resonance depth imaging [33], and typical measured $T_{1,\mathrm{int}}$ times are about 1–4 ms at room temperature.

III. GADOLINIUM-NV RELAXOMETRY

We first show that positioning the Gd-coated tip in close proximity to a shallow NV center can reproducibly change its relaxation time. Figure 2(b) shows the T_1 relaxation curves for a single NV at two tip positions centered above the NV center (blue) and 5 μm laterally displaced from the NV (orange). At a tip-NV separation of 5 μm, the tip is sufficiently far away such that $T_1 = T_{1,\mathrm{int}}$. By positioning the tip within tens of nanometers of the NV, we observe an almost 3 orders of magnitude reduction in T_1, from 4.4 ms to 8.8 μs. This measurement can be cycled with consistent results, which provides verification that the surface is not becoming contaminated with Gd and that the tip retains its integrity; both are critical requirements for faithful imaging. We note that at incident laser powers above 1 mW, positioning the tip over the NV results in a permanent reduction of T_1, which we attribute to desorption of Gd from the tip via excess heating. The fact that T_1 retains its reduced value below 10 μs after the removal of the silicon tip suggests that the silicon is not significantly contributing to the measured T_1 reduction.

The measurement of the full relaxation curve shown in Fig. 2(b) can take many hours, limited mainly by photon shot noise, which is impractical for imaging experiments. Data acquisition time is of heightened importance for two- or three-dimensional imaging, as the number of data points scales rapidly as the spatial resolution is increased. Furthermore, it is difficult to keep the tip-NV separation stable in ambient conditions with traditional AFM techniques over these time scales, due mainly to thermal drift. To reduce data acquisition time and mitigate measurement errors induced by thermal drift, we sample only a small subset of τ points on the curve in Fig. 2(b) when imaging. The set of τ points we use is judiciously chosen to maximize the signal-to-noise ratio (SNR). It is straightforward to show that the SNR is maximized for a fixed τ approximately equal to T_1. However, when performing scanning measurements, T_1 can vary across the sample by many orders of magnitude, and, hence, different τ values optimize the SNR at different positions in the scan.

A two-dimensional map of the NV T_1 versus tip position is presented in Fig. 3. There is a clear and highly localized reduction in T_1 near the center of the scan that indicates the location of closest approach between the Gd-coated tip and the NV center. As expected, the T_1 increases as the tip-NV separation is increased until the original $T_{1,\mathrm{int}}$ of the NV center is observed along the periphery of the scan area. The observation of $T_{1,\mathrm{int}}$ is important because it indicates that there is no significant Gd contamination on the diamond surface during the scan. To mitigate thermal drift observed to be approximately 1 nm/ min, after each pixel an image registration algorithm [34] is used to realign the tip with the NV center. The alignment image is provided by the near-field optical profile of the NV photoluminescence (PL) in

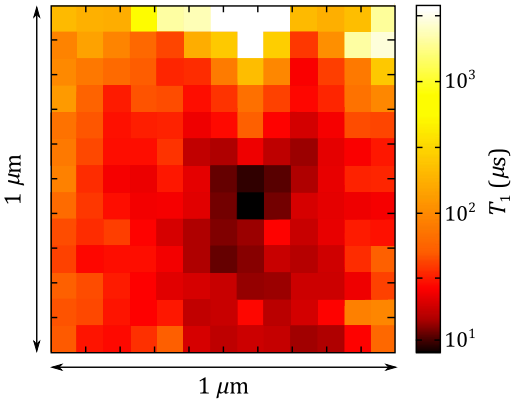

FIG. 3. Two-dimensional map of the T_1 relaxation time of the NV center versus Gd-coated tip position. The T_1 times are inferred from fixed τ measurements with $\tau = 4, 8, 40, 80, 400, 800$ μs at each pixel. The distinct reduction in T_1 in the center of the image indicates the closest approach of the tip to the NV. The spatial resolution of the scan (75 nm per pixel) is chosen to limit the measurement time; a higher-resolution one-dimensional line scan is shown in Fig. 4.

the presence of the tip, which allows for a reproducible alignment with a maximum error of 10 nm.

The image in Fig. 3 is compiled from a set of measurements with $\tau = 4, 8, 40, 80, 400, 800$ μs, which span the range of T_1 times accessible in the scan area. To generate a T_1 image from the fixed τ measurements, a fit to an exponential decay is performed for the data taken at each fixed τ. The T_1 times extracted from the six fixed τ measurements are then averaged, weighted by the error in their respective fit, to arrive at a final T_1 time that is plotted in the image. The T_1 exponential fit is complicated by the dependence of the measured PL on tip position due to a combination of shadowing and near-field effects from the tip and a reduced PL when T_1 becomes comparable to the sub-μs metastable-state relaxation time [19]. Therefore, at each tip position the steady-state PL under laser excitation is measured and included in the T_1 fit.

Figure 4(a) shows a one-dimensional line cut of a single $\tau = 8$ μs measurement in Fig. 3 taken through the location of the NV center. In order to maximize the SNR when the tip is near the NV, we choose this fixed τ value to be around 8.8 μs, the expected T_1 when the tip is near the NV from Fig. 2(b). Plotted on the vertical axis is the percentage change in PL at each tip position. This change defined as $[\mathrm{PL(sig)}/\mathrm{PL(ref)} - 1]$, and heretofore referred to as contrast, is equal to zero if the NV is polarized in the $|0\rangle$ state and becomes negative as the NV evolves into an unpolarized state. The one-dimensional color plots in Fig. 4(b) show how the fixed τ contrast changes with choice of τ. At $\tau = 0$ μs, the state of the NV is polarized at all tip positions, resulting in little contrast across the entire scan. Increasing τ to 4 μs begins to reveal contrast in the center of the line scan where the NV T_1 is the shortest, while the contrast remains near zero at the extremes of the line scan where T_1

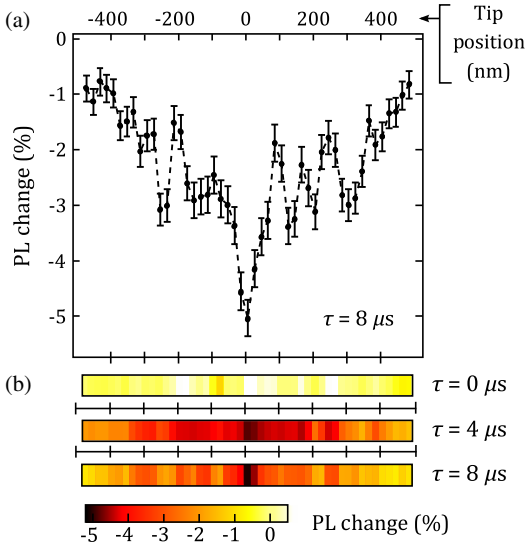

FIG. 4. (a) One-dimensional line scan of the data in Fig. 3, showing the measured PL change for a fixed dark time $\tau = 8\ \mu$s. The error bars are computed from two consecutive line scans with nearest-neighbor averaging and are attributed to photon shot noise and tip drift. (b) Line scans for $\tau = 0, 4, 8\ \mu$s. There is no discernible contrast at $\tau = 0\ \mu$s, but at longer τ, there is a clear reduction in T_1 at the center of the line scan that depends sharply on tip position. The total data acquisition time at each tip position is 6 min.

is the longest. The contrast at the center of the line scan is further enhanced at $\tau = 8\ \mu$s, where $T_1 \approx \tau$.

Figure 5 plots T_1 as a function of tip position zoomed in to a 300-nm-wide region in the center of Fig. 4. In this case,

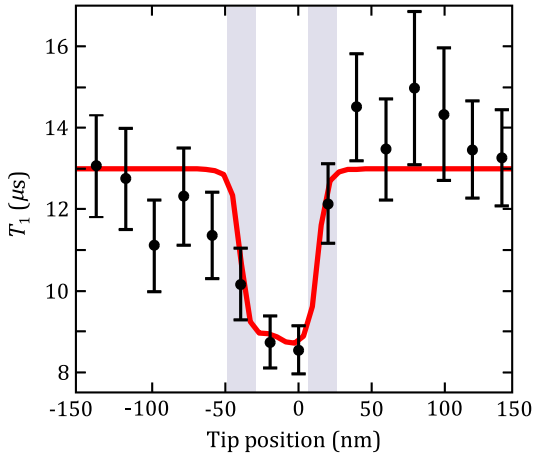

FIG. 5. Extracted T_1 times from the data presented in Fig. 4. The spatial resolution is limited by the 20-nm point spacing and is in good agreement with the resolution deduced from the change in T_1 versus tip position in comparison to the magnitude of the vertical error bars. The shaded blue regions are 20-nm-wide guides to the eye. The data are modeled by a simulation that computes, as a function of scan position, the magnetic field from a finite 50 nm × 50 nm surface of Gd. The result (red solid line) indicates a Gd density of 11.4 spins/nm^2 for a NV depth of 10 nm.

T_1 is extracted from a fit to the $\tau = 4, 8\ \mu$s data shown in Fig. 4, as these fixed τ points provide the best estimate for T_1 in this range. The data show an approximately 50-nm-wide feature, and, importantly, from the slope of the feature edges, a spatial resolution estimated to be 20 nm. This spatial resolution is set by the 20-nm scan step size, which is chosen to be slightly larger than the combined effect of approximately 10-nm AFM drift and approximately 10-nm repeatability of the image registration algorithm used per point. Pushing to higher spatial resolution will require first an improvement in the AFM drift during the measurement and eventually shallower NV centers.

IV. SIMULATIONS

The 50-nm-wide plateau of reduced T_1 in the center of Fig. 5 represents a region of the tip with locally enhanced Gd concentration over a background, the densities of which can be estimated from a simulation shown in the red trace. The model for our simulation places a two-dimensional layer of discrete Gd ions of uniform background concentration on a plane, with a region of locally elevated Gd concentration that measures 50 nm × 50 nm and computes the magnetic field the NV will experience from the ensemble of Gd spins at each scan position. Assuming the Gd samples all $\{|m_s\rangle\}$ in the $S = 7/2$ Hilbert space in a thermal mixture with equal spin populations, we compute the mean-square perpendicular magnetic field the NV experiences from each Gd spin, $\langle[\mathbf{B}_\perp(\mathbf{r})]^2\rangle$. In this expression, $\langle\ldots\rangle$ denotes a mean-square average over the $\{|m_s\rangle\}$ subspace taken by a trace over the density matrix of the mixed state. The magnetic field from a single Gd spin is given by

$$\mathbf{B}(\mathbf{r}) = \frac{\mu_0}{4\pi}\frac{g_{\mathrm{Gd}}\mu_B}{|\mathbf{r}|^3}\left[\mathbf{S} - \frac{3\mathbf{r}(\mathbf{r}\cdot\mathbf{S})}{|\mathbf{r}|^2}\right], \tag{2}$$

where $\mathbf{S}$ is the Gd electron spin vector, $g_{\mathrm{Gd}} = 2$ is the Gd electron g factor, and μ_B is the Bohr magneton. The NV relaxation rate due to the fluctuating field of a single Gd spin at position $\mathbf{r}$ is modeled by an Ornstein-Uhlenbeck process and is given by

$$\Gamma_{\mathrm{Gd}}(\mathbf{r}) = \frac{3\tau_c\gamma_{\mathrm{NV}}^2}{1+\omega_{\mathrm{NV}}^2\tau_c^2}\langle[\mathbf{B}_\perp(\mathbf{r})]^2\rangle, \tag{3}$$

where $\gamma_{\mathrm{NV}} = 2\pi \times 28$ GHz/T is the NV electron spin gyromagnetic ratio, and τ_c is the effective correlation time of the Gd noise spectrum taken to be 0.36 ns [35]. With a 10-nm-deep NV, the simulation result in Fig. 5 predicts a background concentration of 7.7 ± 3.3 spins/nm^2, with an additional 3.7 ± 1.4 spins/nm^2 in a 50 nm × 50 nm region of the tip, which reduces T_1 from 13 to 8.8 μs at the center of the line scan. At the tip position that yields the shortest T_1, the simulation predicts that 70% of the measured T_1 reduction is a result of the magnetic field generated by 2600 ± 1500 Gd spins, where the error bars in the density

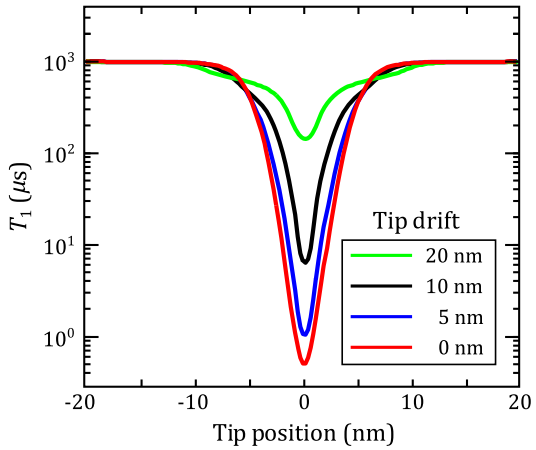

FIG. 6. Simulated T_1 response to a single Gd spin for a 3-nm-deep NV center with $T_{1,\mathrm{int}} = 1$ ms, accounting for various magnitudes of tip drift during the measurement. The minimum T_1 time observed depends strongly on the size of the drift, increasing from 0.50 μs with no drift to 1.04, 6.36, and 145 μs with 5, 10, and 20 nm of drift, respectively.

and number of spins arise from a 2-nm uncertainty in the depth of the NV.

We now turn to a more detailed discussion of spatial resolution and sensitivity, which are intimately related in this experiment. In particular, we focus on the goal of imaging a single Gd spin. Thermal AFM tip drift during the measurement can have dramatic effects, as is evidenced by the simulation results shown in Fig. 6. Plotted are one-dimensional T_1 images simulated with different magnitudes of tip drift for a single Gd target spin, a 3-nm-deep NV center and $T_{1,\mathrm{int}} = 1$ ms. To calculate these results, first the dependence of T_1 on tip position is calculated in the absence of drift shown as the red trace with the largest dip in Fig. 6. When drift is encountered experimentally, the result will be a sampling of many tip positions during the measurement, which serves to blur out the effect of the Gd spin. This can be modeled by taking a sampling of T_1 times around each tip position, with a spatial width equal to the magnitude of the drift during the acquisition time for each measurement point. We can then sum the exponential decay curves of each T_1 time in the sampling area to represent the curve that will be measured experimentally. Although this curve is a sum of exponential decays with different time constants, we can do a least-squares fit to a single exponential decay with one time constant to obtain an averaged T_1 response. Carrying out this procedure for different drift magnitudes of 5, 10, and 20 nm shows a stark reduction in the predicted T_1 response as drift is increased, evident on a log scale. Notably, the shortest measured T_1 time decreases from 145 μs with 20 nm of drift to 0.50 μs with no drift. Using the current experimental parameters of a 10-nm-deep NV, $T_{1,\mathrm{int}} = 4.4$ ms, 10 nm of drift per measurement point, and 70 kcounts/s of photon counts from the NV center, we can use the simulation results to predict a single spin sensitivity that accounts for thermal drift. Under these conditions with a single Gd spin, one predicts a minimum T_1 time of 715 μs and a SNR of 1 to be reached in 30 s of averaging time.

To reach the goal of imaging single Gd spins, we address several areas for improvement, namely, shallower NV centers, reduced thermal drift, and improved photon collection. Using shallower NV centers will provide a much larger signal, since $\Gamma_{\mathrm{Gd}}(r) \sim r^{-6}$ for a single Gd spin. Thermal drift estimated to be about 1 nm/ min in this work can be reduced by using active drift compensation at the expense of measurement complexity, which has been shown to improve drift to 5 pm/ min in ambient conditions [36]. Operating at cryogenic temperatures can also reduce drift significantly but also at the expense of measurement complexity and incompatibility with biological systems. Photon shot noise can be improved by increasing the number of counts from the NV center. In the current geometry, the AFM tip and objective are on the same side of the diamond sample, which leads to partial shadowing of the NV center by the AFM tip. Using a geometry where the objective and AFM tip are on opposite sides of the sample [33] will improve the NV count rate, as well as allow for the use of an oil immersion objective with a large numerical aperture. Alternatively, collection efficiency can be dramatically improved by structuring the diamond with nanopillars, in particular, by using a NV diamond nanopillar as the scanning probe [23,27], though presently, NV spin properties in such nanostructures are poor compared to those in bulk diamond. It is also possible to have greater control of the Gd concentration by utilizing chemically functionalized silicon tips, where ideally a monolayer of Gd complexes can be realized with a tunable areal density.

We now estimate the sensitivity to a single Gd spin for optimized conditions of reduced drift, higher photon counts, and shallower NV centers based on the discussions above. Using a 3-nm-deep NV, $T_{1,\mathrm{int}} = 1$ ms to account for shorter T_1 times typically seen in shallower NV centers [33], 1 nm of drift per measurement point, and 120 kcounts/s from the NV center, one predicts a minimum T_1 time of 0.55 μs and a SNR of 1 to be reached in 10 ms of averaging time. We note that these improvements are realistic: (2–3)-nm-deep NV centers have already been demonstrated as external nuclear spin sensors [37,38], and oil immersion objectives readily achieve such photon count rates. This result demonstrates the feasibility of performing scanning relaxometry with NV centers and provides a roadmap for controllably detecting single Gd electron spins with scanning probe microscopy.

ACKNOWLEDGMENTS

The authors thank K. Ohno and D. D. Awschalom for diamond growth instruction. This work is supported by the

DARPA QuASAR program, the Air Force Office of Scientific Research under Grant No. FA9550-13-1-0198, and the MRSEC Program of the National Science Foundation under Grant No. DMR 1121053. B. A. M. is supported through the Department of Defense (NDSEG).

[1] H. Hegyi and M. Gerstein, The relationship between protein structure and function: A comprehensive survey with application to the yeast genome, J. Mol. Biol. **288**, 147 (1999).

[2] P. C. Lauterbur, M. H. Mendonca-Dias and A. M. Rudin, *Augmentation of Tissue Water Proton Spin-Lattice Relaxation Rates by In Vivo Addition of Paramagnetic Ions*, in Frontiers of Biological Energetics Vol. 1, 3rd ed., edited by P. L. Dutton, J. S. Leigh, and A. Scarpa (Academic Press, New York 1978), p. 752.

[3] D. H. Carr and D. G. Gadian, Contrast agents in magnetic resonance imaging, Clinical Radiology **36**, 561 (1985).

[4] H. J. Weinmann, R. C. Brasch, W. R. Press, and G. E. Wesbey, Characteristics of gadolinium-DTPA complex: A potential NMR contrast agent, AJR Am. J. Roentgenol. **142**, 619 (1984).

[5] C.-H. Huang and A. Tsourkas, Gd-based macromolecules and nanoparticles as magnetic resonance contrast agents for molecular imaging, Curr. Top. Med. Chem. **13**, 411 (2013).

[6] R. Di Corato, F. Gazeau, C. Le Visage, D. Fayol, P. Levitz, F. Lux, D. Letourneur, N. Luciani, O. Tillement, and C. Wilhelm, High-resolution cellular MRI: Gadolinium and iron oxide nanoparticles for in-depth dual-cell imaging of engineered tissue constructs, ACS Nano **7**, 7500 (2013).

[7] M. F. Kircher, A. de la Zerda, J. V. Jokerst, C. L. Zavaleta, P. J. Kempen, E. Mittra, K. Pitter, R. Huang, C. Campos, F. Habte, R. Sinclair, C. W. Brennan, I. K. Mellinghoff, E. C. Holland, and S. S. Gambhir, A brain tumor molecular imaging strategy using a new triple-modality MRI-photoacoustic-Raman nanoparticle, Nat. Med. **18**, 829 (2012).

[8] S. Serres, M. S. Soto, A. Hamilton, M. A. McAteer, W. S. Carbonell, M. D. Robson, O. Ansorge, A. Khrapitchev, C. Bristow, L. Balathasan, T. Weissensteiner, D. C. Anthony, R. P. Choudhury, R. J. Muschel, and N. R. Sibson, Molecular MRI enables early and sensitive detection of brain metastases, Proc. Natl. Acad. Sci. U.S.A. **109**, 6674 (2012).

[9] A. Potapov, H. Yagi, T. Huber, S. Jergic, N. E. Dixon, G. Otting, and D. Goldfarb, Nanometer-scale distance measurements in proteins using Gd^{3+} spin labeling, J. Am. Chem. Soc. **132**, 9040 (2010).

[10] D. T. Edwards, Z. Ma, T. J. Meade, D. Goldfarb, S. Han, and M. S. Sherwin, Extending the distance range accessed with continuous wave EPR with Gd^{3+} spin probes at high magnetic fields, Phys. Chem. Chem. Phys. **15**, 11313 (2013).

[11] V. V. Dobrovitski, G. D. Fuchs, A. L. Falk, C. Santori, and D. D. Awschalom, Quantum control over single spins in diamond, Annu. Rev. Condens. Matter Phys. **4**, 23 (2013).

[12] S. Kaufmann, D. A. Simpson, L. T. Hall, V. Perunicic, P. Senn, S. Steinert, L. P. McGuinness, B. C. Johnson, T. Ohshima, F. Caruso, J. Wrachtrup, R. E. Scholten, P. Mulvaney, and L. Hollenberg, Detection of atomic spin labels in a lipid bilayer using a single-spin nanodiamond probe, Proc. Natl. Acad. Sci. U.S.A. **110**, 10894 (2013).

[13] G. Kucsko, P. C. Maurer, N. Y. Yao, M. Kubo, H. J. Noh, P. K. Lo, H. Park, and M. D. Lukin, Nanometre-scale thermometry in a living cell, Nature (London) **500**, 54 (2013).

[14] L. Rondin, J.-P. Tetienne, T. Hingant, J.-F. Roch, P. Maletinsky, and V. Jacques, Magnetometry with nitrogen-vacancy defects in diamond, Rep. Prog. Phys. **77**, 056503 (2014).

[15] J. H. Cole and L. C. L. Hollenberg, Scanning quantum decoherence microscopy, Nanotechnology **20**, 495401 (2009).

[16] E. Schäfer-Nolte, L. Schlipf, M. Ternes, F. Reinhard, K. Kern, and J. Wrachtrup, Tracking temperature-dependent relaxation times of individual ferritin nanomagnets with a wideband quantum spectrometer, Phys. Rev. Lett. **113**, 217204 (2014).

[17] D. H. Carr, J. Brown, G. M. Bydder, R. E. Steiner, H. J. Weinmann, U. Speck, A. S. Hall, and I. R. Young, Gadolinium-DTPA as a contrast agent in MRI: Initial clinical experience in 20 patients, AJR Am. J. Roentgenol. **143**, 215 (1984).

[18] S. Steinert, F. Ziem, L. T. Hall, A. Zappe, M. Schweikert, N. Götz, A. Aird, G. Balasubramanian, L. Hollenberg, and J. Wrachtrup, Magnetic spin imaging under ambient conditions with sub-cellular resolution, Nat. Commun. **4**, 1607 (2013).

[19] J.-P. Tetienne, T. Hingant, L. Rondin, A. Cavaillès, L. Mayer, G. Dantelle, T. Gacoin, J. Wrachtrup, J.-F. Roch, and V. Jacques, Spin relaxometry of single nitrogen-vacancy defects in diamond nanocrystals for magnetic noise sensing, Phys. Rev. B **87**, 235436 (2013).

[20] A. O. Sushkov, N. Chisholm, I. Lovchinsky, M. Kubo, P. K. Lo, S. D. Bennett, D. Hunger, A. Akimov, R. L. Walsworth, H. Park, and M. D. Lukin, , All-optical sensing of a single-molecule electron spin, Nano Lett. **14**, 6443 (2014).

[21] F. C. Ziem, N. S. Götz, A. Zappe, S. Steinert, and J. Wrachtrup, Highly sensitive detection of physiological spins in a microfluidic device, Nano Lett. **13**, 4093 (2013).

[22] A. Ermakova, G. Pramanik, J.-M. Cai, G. Algara-Siller, U. Kaiser, T. Weil, Y.-K. Tzeng, H. C. Chang, L. P. McGuinness, M. B. Plenio, B. Naydenov, and F. Jelezko, Detection of a few metallo-protein molecules using color centers in nanodiamonds, Nano Lett. **13**, 3305 (2013).

[23] P. Maletinsky, S. Hong, M. S. Grinolds, B. Hausmann, M. D. Lukin, R. L. Walsworth, M. Loncar, and A. Yacoby, A robust scanning diamond sensor for nanoscale imaging with single nitrogen-vacancy centres, Nat. Nanotechnol. **7**, 320 (2012).

[24] L. Rondin, J.-P. Tetienne, P. Spinicelli, C. Dal Savio, K. Karrai, G. Dantelle, A. Thiaville, S. Rohart, J.-F. Roch, and V. Jacques, Nanoscale magnetic field mapping with a single spin scanning probe magnetometer, Appl. Phys. Lett. **100**, 153118 (2012).

[25] L. Rondin, J.-P. Tetienne, S. Rohart, A. Thiaville, T. Hingant, P. Spinicelli, J.-F. Roch, and V. Jacques, Stray-field imaging of magnetic vortices with a single diamond spin, Nat. Commun. **4**, 2279 (2013).

[26] T. Häberle, D. Schmid-Lorch, K. Karrai, F. Reinhard, and J. Wrachtrup, High-dynamic-range imaging of nanoscale magnetic fields using optimal control of a single qubit, Phys. Rev. Lett. **111**, 170801 (2013).

[27] M. S. Grinolds, S. Hong, P. Maletinsky, L. Luan, M. D. Lukin, R. L. Walsworth, and A. Yacoby, Nanoscale magnetic imaging of a single electron spin under ambient conditions, Nat. Phys. **9**, 215 (2013).

[28] T. Häberle, D. Schmid-Lorch, F. Reinhard, and J. Wrachtrup, Scanning probe microscopy with chemical contrast by nanoscale nuclear magnetic resonance, arXiv: 1406.3324.

[29] D. Rugar, H. J. Mamin, M. H. Sherwood, M. Kim, C. T. Rettner, K. Ohno, and D. D. Awschalom, Proton magnetic resonance imaging with a nitrogen-vacancy spin sensor, arXiv:1406.2983.

[30] E. van Oort, N. B. Manson, and M. Glasbeek, Optically detected spin coherence of the diamond N-V centre in its triplet ground state, J. Phys. C **21**, 4385 (1988).

[31] K. Ohno, F. J. Heremans, L. C. Bassett, B. A. Myers, D. M. Toyli, A. C. Bleszynski Jayich, C. J. Palmstrom, and D. D. Awschalom, Engineering shallow spins in diamond with nitrogen delta-doping, Appl. Phys. Lett. **101**, 082413 (2012).

[32] K. Ohashi, T. Rosskopf, H. Watanabe, M. Loretz, Y. Tao, R. Hauert, S. Tomizawa, T. Ishikawa, J. Ishi-Hayase, S. Shikata, C. L. Degen, and K. M. Itoh, Negatively charged nitrogen-vacancy centers in a 5 nm thin ^{12}C diamond film, Nano Lett. **13**, 4733 (2013).

[33] B. A. Myers, A. Das, M. C. Dartiailh, K. Ohno, D. D. Awschalom, and A. C. Bleszynski Jayich, Probing surface noise with depth-calibrated spins in diamond, Phys. Rev. Lett. **113**, 027602 (2014).

[34] M. Guizar-Sicairos, S. T. Thurman, and J. R. Fienup, Efficient subpixel image registration algorithms, Opt. Lett. **33**, 156 (2008).

[35] H.-K. Kim, G.-H. Lee, T.-J. Kim, and Y.-M. Chang, Determination of correlation times of new paramagnetic gadolinium MR contrast agents by EPR and ^{17}O NMR, Bull. Korean Chem. Soc. **30**, 849 (2009).

[36] G. M. King, A. R. Carter, A. B. Churnside, L. S. Eberle, and T. T. Perkins, Ultrastable atomic force microscopy: atomic-scale stability and registration in ambient conditions, Nano Lett. **9**, 1451 (2009).

[37] M. Loretz, S. Pezzagna, J. Meijer, and C. L. Degen, Nanoscale nuclear magnetic resonance with a 1.9-nm-deep nitrogen-vacancy sensor, Appl. Phys. Lett. **104**, 033102 (2014).

[38] C. Müller, X. Kong, J.-M. Cai, K. Melentijević, A. Stacey, M. Markham, D. Twitchen, J. Isoya, S. Pezzagna, J. Meijer, J. F. Du, M. B. Plenio, B. Naydenov, L. P. McGuinness, and F. Jelezko, Nuclear magnetic resonance spectroscopy with single spin sensitivity, Nat. Commun. **5**, 4703 (2014).